

Vertically Illuminated, Resonant Cavity Enhanced, Graphene–Silicon Schottky Photodetectors

Maurizio Casalino,[†] Ugo Sassi,[‡] Ilya Goykhman,[‡] Anna Eiden,[‡] Elefterios Lidorikis,[§] Silvia Milana,[‡] Domenico De Fazio,[‡] Flavia Tomarchio,[‡] Mario Iodice,[†] Giuseppe Coppola,[†] and Andrea C. Ferrari^{*,‡,§}

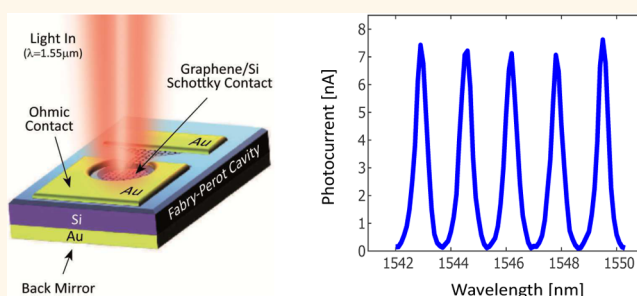
[†]Institute for Microelectronics and Microsystems, National Research Council, 80131 Naples, Italy

[‡]Cambridge Graphene Centre, University of Cambridge, Cambridge CB3 0FA, U.K.

[§]Department of Materials Science and Engineering, University of Ioannina, Ioannina 45110, Greece

ABSTRACT: We report vertically illuminated, resonant cavity enhanced, graphene–Si Schottky photodetectors (PDs) operating at 1550 nm. These exploit internal photoemission at the graphene–Si interface. To obtain spectral selectivity and enhance responsivity, the PDs are integrated with an optical cavity, resulting in multiple reflections at resonance, and enhanced absorption in graphene. We get a wavelength-dependent photoresponse with external (internal) responsivity ~ 20 mA/W (0.25A/W). The spectral selectivity may be further tuned by varying the cavity resonant wavelength. Our devices pave the way for developing high responsivity hybrid graphene–Si free-space illuminated PDs for optical communications, coherence optical tomography, and light-radars.

KEYWORDS: graphene, photodetectors, resonant cavity, internal photoemission



Near infrared (NIR) photodetection at 1550 nm is of paramount importance for a variety of applications, ranging from optical communications^{1–4} to remote sensing.^{5,6} In modern telecom systems, operation at 1550 nm benefits from a reduced light absorption in optical fibers.¹ In free-space optical communications (FSO)^{2–4} and light-radars (LIDARs),^{5,6} this minimizes the propagation losses in fog³ and humid conditions,⁴ due to lower optical absorption and scattering compared to wavelengths $< 1 \mu\text{m}$, and improves eye safety because the outer layer of the eye (cornea) absorbs light at 1550 nm and does not allow it to focus on the retina.^{3,5} In optical coherence tomography (OCT), a noninvasive imaging technique for biological tissues,⁷ the advantages of using 1550 nm are enhanced penetration depth, due to lower scattering in tissue with respect to shorter wavelengths,⁷ and enhanced imaging contrast at deeper penetration depths, where multiscattering processes dominate.⁷

Many photodetectors (PDs) for 1550 nm have been proposed.^{1,8–10} For telecom and datacom applications, these typically rely on a waveguide configuration,^{11–20} in which optical confinement and guiding contribute to enhanced light absorption and photodetection. On the other hand, for FSO, OCT and LIDARs, NIR PDs for free-space illumination are required.^{2–7} At present, III–V compound (e.g., InGaAs, InP)^{21,22} and group IV (Ge)^{11–14} semiconductors are the

materials of choice for vertically illuminated NIR PDs, due to their high ($>90\%$)⁸ NIR absorption. The ever growing demand and performance requirements in modern systems (such as bit-rate, number of pixels, imaging matrix size, operation and processing speed)^{1,8} make it crucial to integrate PDs with supporting circuitry (drivers, amplifiers, processors) on the same chip. Since modern microelectronics relies on mature complementary metal-oxide-semiconductor (CMOS) technology, the development of NIR PDs on Si is promising for integrated microsystems, combining both optical and electronic functionalities. III–V materials are not compatible with standard CMOS fabrication processes because of cross-contamination and dopant redistribution effects,²³ and are typically manufactured in separate facilities.²³ They can be later bonded with CMOS chips using advanced packaging and assembling.²⁴ However, the overall performance can degrade due to packaging parasitics (e.g., parasitic capacitance and inductance) and cross-talks associated with the wire-bond leads.²⁴ Epitaxially grown Ge on Si provides a competitive platform to InGaAs and InP based NIR photodetection.^{13,25,26} Nevertheless, due to defects²³ and dislocations-like recomb-

Received: July 8, 2017

Accepted: October 25, 2017

Published: October 26, 2017

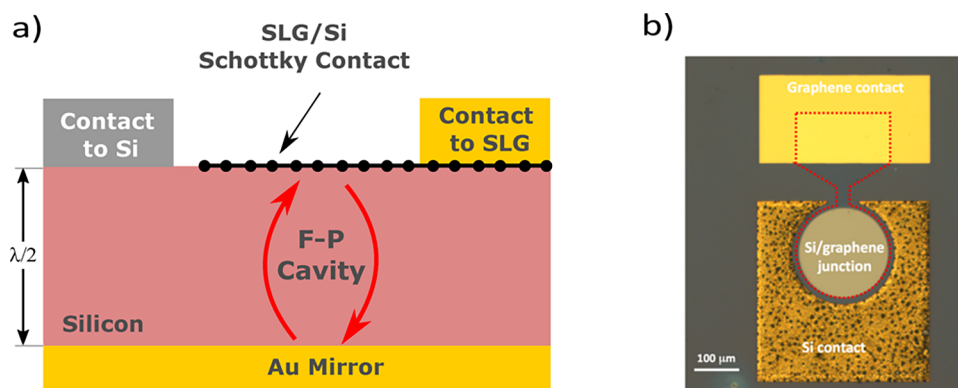


Figure 1. (a) Schematic cross-section of our resonant cavity enhanced (RCE) SLG/Si Schottky PD under illumination. (b) Optical image of fabricated device.

nation centers at the Si–Ge interface,^{13,25,26} these PDs typically show larger leakage current²⁶ and smaller shunt resistance²⁶ compared to III–V devices, resulting in increased noise (thermal and shot).¹³ To reduce the defects density, a two-step Ge deposition is commonly used;^{13,25,26} however, it involves high (>650 °C) temperature processes²⁶ that can sacrifice the thermal budget, which limits the amount of thermal energy available to the wafer during the fabrication process.

An alternative and promising approach for monolithic integration of NIR PDs with CMOS electronics is to perform sub-bandgap photodetection in Si exploiting the internal photoemission process (IPE) in a Schottky junction.^{8,27–29} In this case, photoexcited carriers from the metal electrode can be emitted to Si over the Schottky barrier Φ_B , allowing NIR detection for photon energy $h\nu > \Phi_B$.^{8,27,28} Schottky PDs have been successfully used in IR focal plane arrays (FPA),³⁰ monolithically integrated with CMOS readout electronics and charge coupled devices (CCDs).⁸ The advantages of the Schottky junction configuration over other PD types (pn and pin junctions, quantum wells) stem from its simple structure,⁸ easy fabrication and integration with CMOS technology.⁸ The main drawback is the limited (<1%)^{31,32} internal quantum efficiency (IQE) of the IPE process, defined as the number of carriers emitted to Si per absorbed photon. This is mainly because the momentum mismatch between the electron states in the metal and Si results in a specular reflection of excited electrons at the Schottky interface.^{8,31} The IQE is linked to the PD internal (external) responsivity R_{int} (R_{ext}), defined as the ratio between the photocurrent I_{ph} and the absorbed (incident) optical power P_{abs} (P_{inc}), i.e., $R_{\text{int}} = I_{\text{ph}}/P_{\text{abs}} = \text{IQE} \cdot q/h\nu$ and $R_{\text{ext}} = I_{\text{ph}}/P_{\text{inc}} = A \cdot R_{\text{int}}$ ⁸ where q is the electron charge and A is the absorptance. As a result, limited IQE leads to limited responsivity, so that the highest R_{ext} reported so far in vertically illuminated Si Schottky PDs operating at 1550 nm is ~ 5 mA/W,³³ much lower than the 0.5–0.9A/W for III–V⁸ and Ge⁸ based PDs. Graphene/Si Schottky PDs at 1550 nm have been demonstrated both in free-space³⁴ and guided mode configurations,^{35,36} with R_{ext} up to 10 mA/W and 0.37A/W respectively. In these devices, a single layer graphene (SLG) acts as electrode in contact with Si, forming a Schottky junction with rectifying characteristics.^{37–39} In general, graphene is an attractive material for photonics and optoelectronics.^{40–43} Its integration with Si may allow the development of miniaturized and cost-effective hybrid optical devices and functionalities.^{44,45} In the case of SLG/Si Schottky PDs, SLG integration allows

absorption of NIR photons with energy below the Si bandgap in close proximity to the Schottky interface,^{34–37} leading to increased IPE IQE. However, the SLG absorption in NIR is $\sim 2.3\%$,^{46,47} and the vast majority of optical power does not contribute to photodetection. As a result, vertically illuminated SLG/Si Schottky PDs have a limited $R_{\text{ext}} \sim 10$ mA/W³⁴ at 1550 nm, over 1 order of magnitude lower compared to $R_{\text{ext}} \sim 0.37\text{A/W}$ ³⁶ for the waveguide-integrated configuration, in which light is fully absorbed in SLG upon optical guiding.

Here we increase R_{ext} of free-space illuminated graphene/Si Schottky PDs by combining a Schottky junction with an optical Fabry–Perot (F–P) cavity to enhance light interaction and absorption at the SLG/Si interface. We show that the PD spectral response and responsivity peaks coincide with F–P resonances, with R_{ext} increasing with the number of light round trips inside the cavity. Taking advantage of multiple (~ 5) light reflections at resonance, we obtain spectrally selective photo-response with maximum R_{ext} (R_{int}) ~ 20 mA/W (0.25A/W), the highest reported so far for vertically illuminated Si PDs at 1550 nm. Our devices pave the way for high responsivity hybrid graphene/Si PDs for NIR.

RESULTS

Figure 1 illustrates our F–P cavity integrated SLG/Si Schottky PD. The resonant structure consists of a $\lambda/2$ Si slab layer confined between SLG/Si top and Au bottom mirrors. When vertically illuminated at resonance, light circulates inside the cavity leading to increased absorption at the SLG/Si interface, resulting in enhanced IPE from SLG to Si. **Figure 2** shows a simulation of SLG absorption in the integrated F–P cavity PD. For this we use the transfer matrix method⁴⁸ and a cavity length $L = 200 \mu\text{m}$. The Au permittivity $\epsilon_{\text{Au}} = -115 + 11.3i$ (at 1550 nm) is assumed to follow the Drude model including damping.⁴⁹ The permittivity of SLG $\epsilon_{\text{SLG}} = 1.8 + 16.4i$ (at 1550 nm) is calculated from its optical conductivity σ , i.e., $\epsilon = 1 + i\sigma/(\omega \cdot \epsilon_0 \cdot \Delta)$, where ω is the angular frequency, ϵ_0 is the permittivity of vacuum, and $\Delta = 0.35$ nm is the SLG thickness. $\sigma = 61 - 4.3i$ [μS] includes contributions from inter- and intraband transitions,^{50,51} assuming a SLG doping ~ 0.25 eV and scattering time ~ 50 fs.

The simulation indicates that the absorption peaks are spaced by 1.65 nm (**Figure 2**), matching the free-spectral range (FSR) of the F–P cavity:^{1,52} $\text{FSR} = \lambda_0^2/(2 \cdot n_g \cdot L)$, where λ_0 is the illumination wavelength, $n_g = n - \lambda_0 \cdot dn/d\lambda$ is the group index of Si around 1550 nm, estimated to be $n_g \sim 3.61$,⁵³ $n = 3.45$ is the refractive index of Si at 1550 nm,⁵³ and $dn/d\lambda$ is the

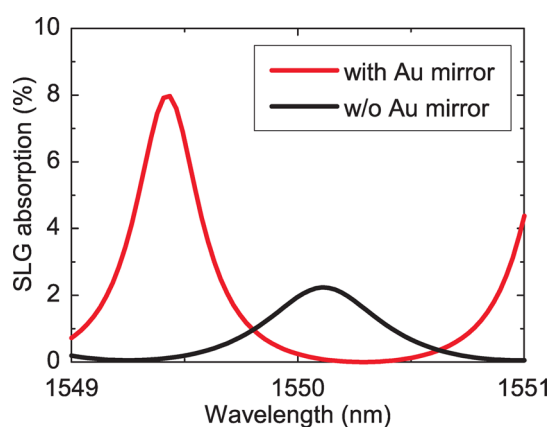


Figure 2. Calculated SLG absorption on top of a cavity with (red) and without (black) Au mirror.

dispersion. We get peak absorptances ~ 2.2 and 8.5% for finesse (*i.e.*, ratio between FSR and resonance line width) of 3 and 5.3 without and with Au mirror, respectively (Figure 2). The peak absorptance for the larger finesse (Au mirror) is ~ 4 times higher than that for the lower finesse (Si/air mirror), due to larger number of light round trips and optical energy build-up inside the F–P cavity.

The device fabrication process is presented in Figure 3 and described in Methods. The PDs are fabricated on a double-polished, low-doped ($N_A \sim 10^{15} \text{cm}^{-3}$, p-type, Boron), $200 \mu\text{m}$ thick Si substrate to minimize the scattering and free-carriers losses in the F–P cavity. SLG is grown by chemical vapor deposition (CVD) on a $35 \mu\text{m}$ -thick Cu foil, following the process described in ref 54. We monitor the SLG quality by using Raman spectroscopy (see Methods) throughout the entire fabrication process Figure 4 (*i.e.*, as grown material, after transfer and after complete device fabrication). Figure 4b

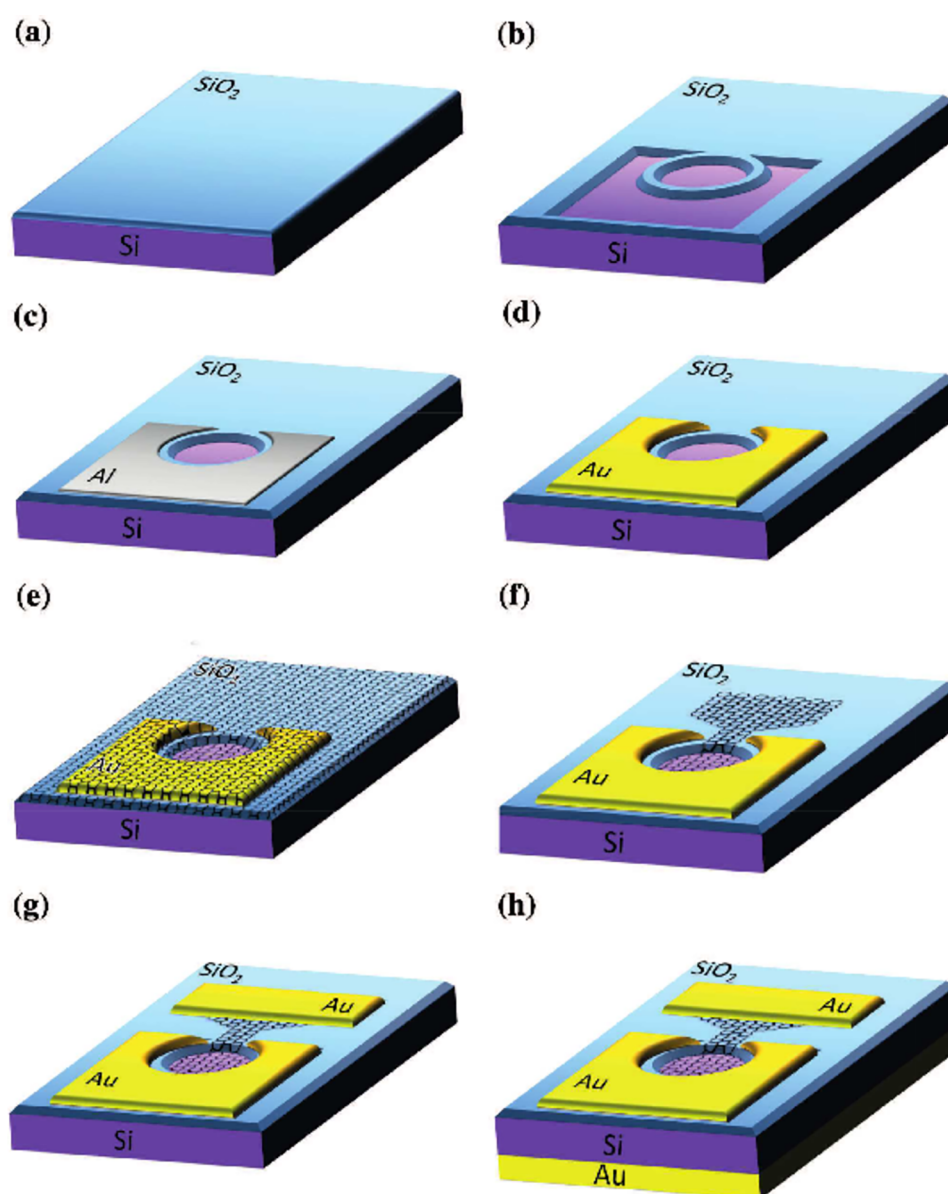


Figure 3. Fabrication process of RCE Si-SLG Schottky PD. (a) SiO_2 layer deposition. (b) Schottky and Ohmic contacts area definition. (c) Al ohmic contact formation. (d) Au protection layer deposition. (e) SLG transfer. (f) SLG shaping. (g) Au contact to SLG deposition. (h) Au Back mirror deposition.

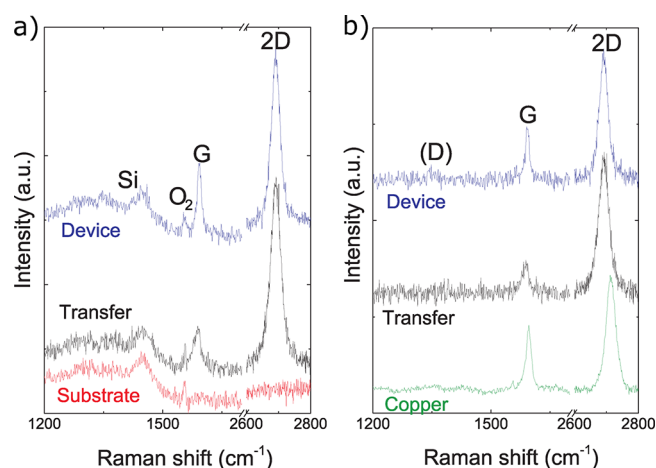


Figure 4. (a) Raman spectra of (red) Si substrate, (black) SLG transferred on Si and (blue) of SLG on Si after device fabrication. (b) Raman spectra after subtraction of the substrate contribution of (green) as-grown SLG on Cu, (black) SLG transferred on Si and (blue) SLG on Si after device fabrication.

(green curve) shows the spectrum of SLG on Cu, after the removal of the background Cu photoluminescence (PL).⁵⁵ The two most intense features are the G and the 2D peak, with no significant D peak. The 2D peak is single-Lorentzian, signature of SLG.⁵⁶ The position of the G peak, Pos(G), is ~ 1595 cm^{-1} , with $\text{fwhm(G)} \sim 9.5$ cm^{-1} . The 2D peak position, Pos(2D) is ~ 2712 cm^{-1} with $\text{fwhm(2D)} \sim 29$ cm^{-1} . The 2D to G peak intensity and area ratios, $I(2D)/I(G)$ and $A(2D)/A(G)$, are ~ 1.9 and 5.8 , respectively. The Raman spectrum of SLG after transfer is shown in Figure 4b, black curve. This is obtained by point-to-point subtraction of the reference Si spectrum (Figure 4a, red curve) from the transferred SLG (Figure 4a, black curve), when the intensities in both spectra are normalized to the third order Si peak at ~ 1450 cm^{-1} .⁵⁷ The 2D peak after transfer is a single-Lorentzian, Pos(2D) ~ 2691 cm^{-1} with $\text{fwhm(2D)} \sim 35$ cm^{-1} . Pos(G) is 1587.5 cm^{-1} with $\text{fwhm(G)} \sim 19.6$ cm^{-1} . The 2D to G peak intensity and area ratios, $I(2D)/I(G)$ and $A(2D)/A(G)$, are 4.32 and 7.16 respectively, suggesting a p-doping $\sim 2.4 \times 10^{12}$ cm^{-2} (~ 200 meV).^{58–60} Figure 4a (blue curve) plots the SLG Raman spectrum after device fabrication and point-to-point subtraction of the Si reference using the same procedure. After device fabrication Pos(G) ~ 1592.4 cm^{-1} , $\text{fwhm(G)} \sim 10.7$ cm^{-1} , Pos(2D) \sim

2691.4 cm^{-1} , $\text{fwhm(2D)} \sim 31.1$ cm^{-1} . $I(2D)/I(G)$ and $A(2D)/A(G)$ are 2.53 and 6.3 respectively, indicating doping $\sim 9 \times 10^{12}$ cm^{-2} (~ 290 meV).^{58–60} We also get $I(D)/I(G) \sim 0.14$, indicating that the fabrication process does introduce some defects in the SLG electrode.^{61,62} To assess the uniformity of the SLG/Si Schottky contact we perform Raman mapping (see Methods). Figure 5 plots the maps of Pos(G) and $I(2D)/I(G)$, confirming that SLG is uniformly located in the device photoactive area (circular area in Figure 5)

Figure 1b shows an optical image of a representative device, where the SLG boundaries are highlighted by a red dashed line. To electrically characterize the PD, we measure the current–voltage (I – V) characteristics of the SLG/Si Schottky junction (Figure 6a) when Si is biased with respect to grounded SLG electrode. The device shows rectifying I – V diode behavior, which follows the Schottky diode equation:^{8,63}

$$I = AA^*T^2 e^{-\Phi_B/k_B T} (e^{qV_a/\eta k_B T} - 1) \quad (1)$$

where $\Phi_B = \Phi_{B0} + \Delta\Phi_B(V)$, Φ_{B0} is the Schottky barrier height (SBH) at zero voltage, $\Delta\Phi_B(V)$ is the SBH change due to applied voltage, A^* is the Richardson constant (32 A/cm^2 K^2 for p-type Si⁸), A is the junction area, $k_B T \sim 26$ meV at room temperature, η is the diode ideality factor, defined as the deviation of the measured I – V curve from the ideal exponential behavior,⁸ and V_a is the applied voltage. In the low injection regime ($V_a < 2$ V), the device shows negligible series resistance, and a good agreement between theory and experiments can be obtained without taking into account in eq 1 of any series resistance, Figure 6a. $\Delta\Phi_B(V)$ is typically dominant in reverse bias because of the higher potential drop on the Schottky junction (V_D), resulting in a more pronounced barrier-lowering Schottky effect^{8,63} and SLG Fermi level shift.^{37,38,63} On the other hand, V_D in forward bias is limited by the built-in voltage, $V_D < V_{bi}$. This means that, at elevated forward biases, the series resistance will dominate the I – V characteristics for any further voltage increase. Therefore, any additional voltage bias supplied by an external source will result in additional voltage drop on the series resistance, so that V_D will remain unchanged, *i.e.*, $\Delta V_D \leq V_{bi}$. In this case, charge variation induced in the SLG electrode is significantly smaller than in reverse bias, where a Schottky diode behaves as a variable capacitor,⁸ therefore V_D can be significantly higher than V_{bi} . Small variation in Schottky barrier height are possible due to Fermi level changes in forward bias,⁶⁴ however we assume $\Phi_B \sim \Phi_{B0}$ for the low injection ($V_a < 2$ V) region in the forward bias. We estimate

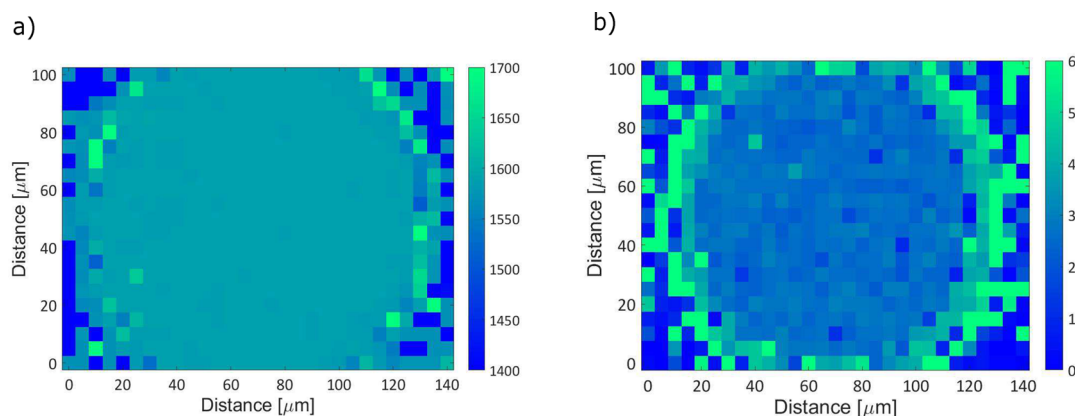


Figure 5. Raman map of SLG/Si Schottky detector. (a) Pos(G). Color bar units [cm^{-1}]. (b) $I(2D)/I(G)$.

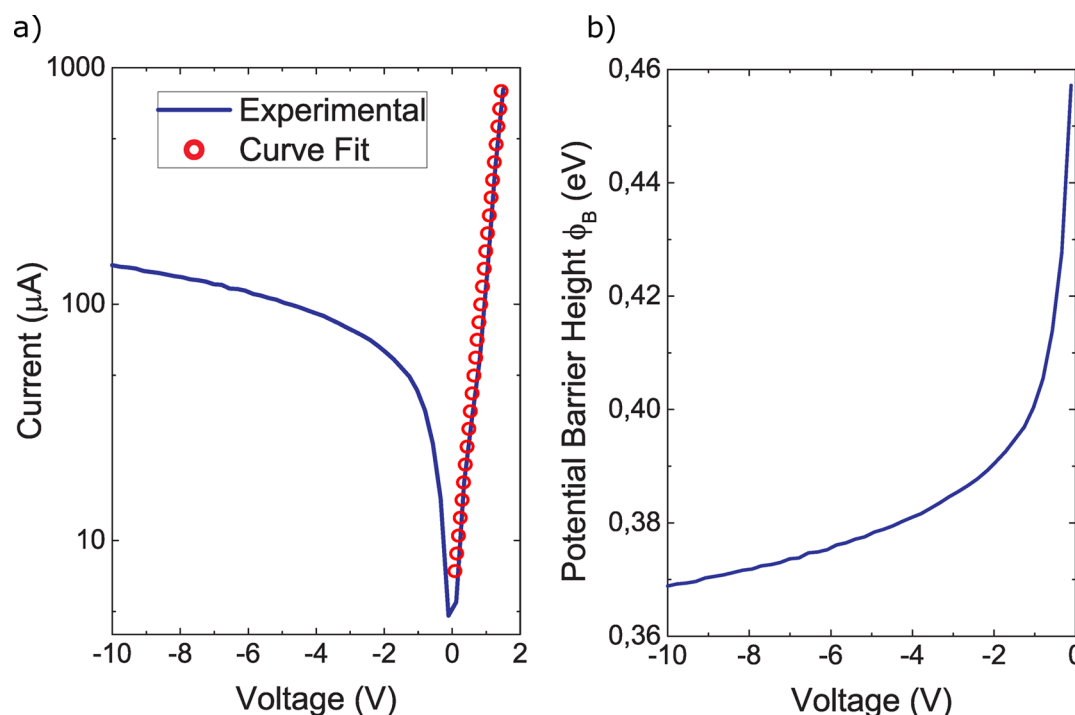


Figure 6. (a) I – V characteristic of SLG/Si Schottky PD (semilog scale). Experimental data and fit are shown. (b) Potential barrier height as a function of reverse bias.

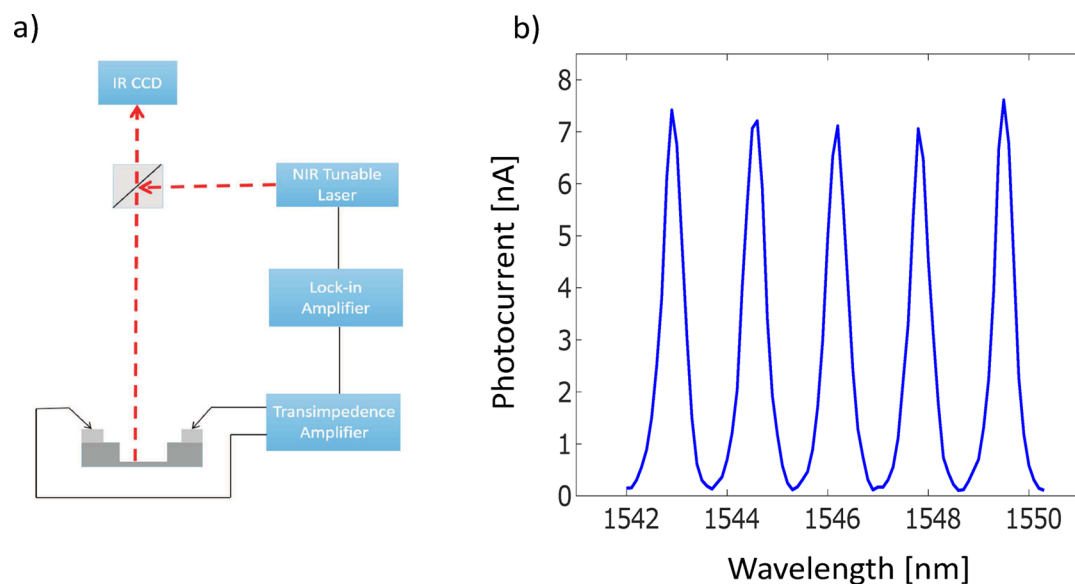


Figure 7. (a) Optoelectronic measurements setup. (b) Spectral response (photocurrent) of RCE SLG/Si Schottky PD without backside Au ($V_R = 1$ V).

SBH in forward bias by fitting the experimental data with eq 1 and using Φ_B and η as fitting parameters. We get $\Phi_B \sim 0.46$ eV and $\eta \sim 11$. These are in the range of previously reported values ($0.41 < \Phi_B < 0.47$ and $2 < \eta < 30$) for SLG/Si Schottky diodes.^{34–39} Φ_{B0} can also be estimated by fitting the reverse current using eq 1 in the limit $V_a \rightarrow 0$. This gives $\Phi_{B0} \sim 0.46$ V. Then, by fitting the I – V curve for entire range of reverse biases, where $\Delta\Phi_B(V)$ cannot be neglected anymore, we obtain the SBH dependence on applied reverse voltage and find $\Delta\Phi_B$ up to ~ 80 meV at $V_R = 10$ V, Figure 6b.

The optoelectronic characterizations are carried out using the setup of Figure 7a (see Methods). Figure 7b plots the spectral

response under reverse voltage $V_R = 1$ V. The device demonstrates spectral selectivity, with wavelength dependent and periodic photocurrent peaks upon illumination. The spectral separation between the peaks is ~ 1.7 nm, matching the FSR = 1.65 nm of the F–P cavity. As expected, at resonance we get photocurrent peaks due to increased absorption at the Schottky interface, Figure 2.

To confirm the cavity effect on PD responsivity, we measure R_{ext} with and without Au mirror, Figure 8a. The slight (~ 0.5 nm) variation in resonant wavelength (Figure 8a,b) is attributed to fabrication tolerances between different devices. We observe a 3-fold R_{ext} enhancement and a spectral (blue)

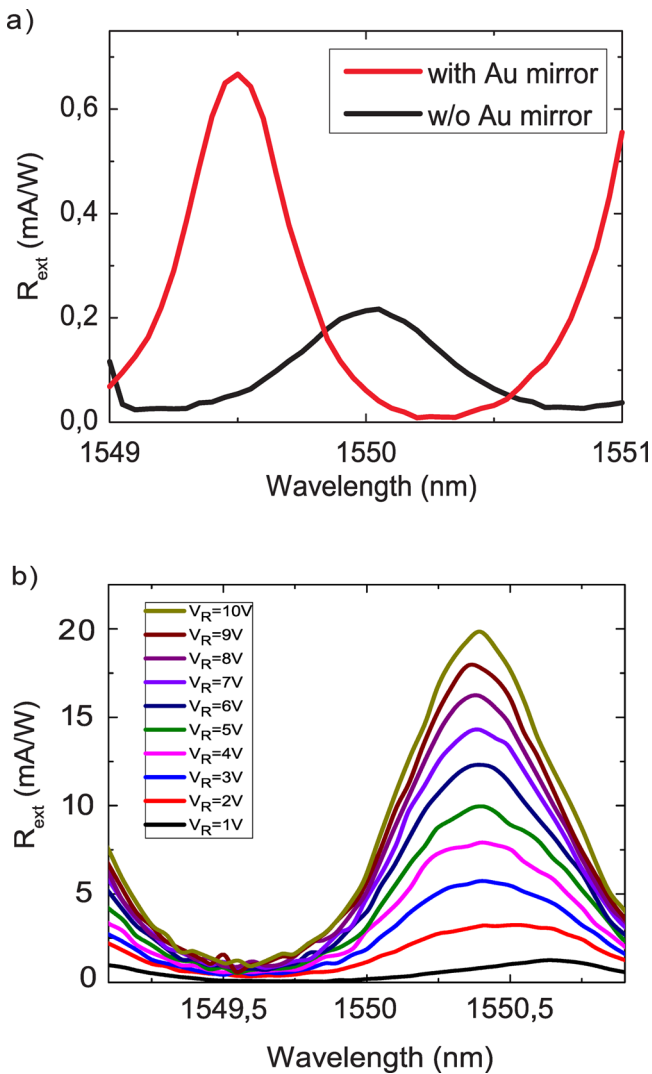


Figure 8. (a) R_{ext} of a SLG-based RCE PD with (red curve) and without (black curve) Au mirror at -1 V. (b) R_{ext} as a function of increased reverse voltage.

shift of resonance wavelengths with the Au mirror compared to the bare Si/air reflector, in agreement with the simulations in Figure 2. As a result, the spectral response of our PDs is tuned accordingly, as for Figure 8a. Thus, the integration of a SLG/Si Schottky detector with a F–P cavity leads to enhanced responsivity, spectral selectivity and wavelength tunability. To further enhance R_{ext} , we exploit the Schottky barrier lowering effect and apply a larger (up to 10 V) reverse bias to the PDs with integrated Au mirrors. Figure 8b plots R_{ext} for different V_R . We get $R_{\text{ext}} \sim 20$ mA/W at $V_R = 10$ V, which corresponds to $R_{\text{int}} \sim 0.25$ A/W, considering the 8% absorption in the SLG electrode. To the best of our knowledge, this is the highest value reported so far for vertically illuminated Schottky Si PDs at 1550 nm. To estimate a noise figure of our PD we calculate the noise equivalent power (NEP), *i.e.*, the amount of incident light power that generates a photocurrent equal to the noise current, $\text{NEP} = i_n/R_{\text{ext}}$.^{1,8} We assume that Johnson (thermal)^{1,8} and shot (quantum) noise^{1,8} dominate over the low-frequency ($1/f$) noise.^{65,66} The Johnson (i_j) and shot (i_s) noise currents normalized to the spectral band [1 Hz] are given by^{1,8} $i_j = ((4kT)/R_{\text{eq}})^{1/2}$ and $i_s = (2q(I_{\text{ph}} + I_d))^{1/2}$, where $R_{\text{eq}} = dV/dI$ is the equivalent resistance of a PD at reverse bias in dark, I_{ph} is

the photocurrent, I_d is the dark current and $i_n = i_j + i_s$. Figure 9 plots NEP as a function of V_R . For $V_R = 10$ V, $R_{\text{ext}} \sim 20$ mA/W,

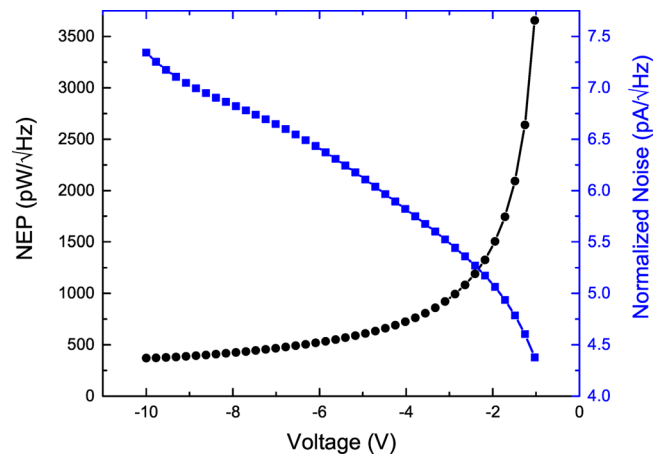


Figure 9. NEP (black circles) and total noise current i_n (blue squares) at different reverse biases.

dark current density ~ 0.47 A/cm² and photoactive area $A = \pi \times 10^{-4}$ cm², we get $i_n \sim 7.4$ pA/Hz^{0.5} and $\text{NEP} \sim 3.5 \times 10^{-10}$ W/Hz^{0.5}. We evaluate a specific detectivity (reciprocal of NEP, used to indicate detection capacity^{1,8}) $D^* = A^{1/2}/\text{NEP} \sim 5.1 \times 10^7$ Jones. NEP and D^* can be improved by decreasing the dark current at the SLG/Si Schottky junction and increasing the responsivity as shown in ref 36. The main factors limiting the time response of cavity integrated Schottky PD are^{8,67} (1) carriers transit time τ_{tr} across the junction depletion region, (2) charge/discharge (RC) time τ_{RC} of the junction capacitance, and (3) cavity photon lifetime τ_{ph} .⁵² Thus, the temporal response of the detector is limited by $\tau = \tau_{\text{tr}} + \tau_{\text{RC}} + \tau_{\text{ph}}$.^{8,67} In our device, (1) the transit time^{8,52} $\tau_{\text{tr}} = x_d/v_{\text{sat}} \sim 36$ ps, where $x_d \sim 3.6$ μm is the depletion region width (at $V_R = 10$ V) and v_{sat} is the carriers saturation velocity in Si (10^7 cm/s⁸), (2) $\tau_{\text{RC}} = R_s C_j \sim 1.35$ ns, where $R_s \sim 1.5$ k Ω is the diode series resistance (extracted from the I – V curve in Figure 6) and $C_j = A \cdot \epsilon_0 \cdot \epsilon_s / x_d \sim 0.9$ pF is the junction capacitance, with $\epsilon_0 = 8.84 \times 10^{-14}$ F/cm the permittivity of vacuum, $\epsilon_s = 11.7$ the dielectric constant of Si and $A = \pi \times 10^{-4}$ cm² the SLG/Si junction area, (3) $\tau_{\text{ph}} = F \cdot L / (\pi \cdot c) \sim 1.1$ ps, with $F = 5.3$ the cavity finesse, $L = 200$ μm the cavity length (Si thickness) and c the speed of light. This gives $\tau \sim \tau_{\text{RC}}$ and RC limited 3 dB roll-off frequency (at which the output power is reduced by 50%) $f_{3\text{dB}} = 1/(2\pi \cdot \tau) \sim 120$ MHz. This can be increased by reducing the device area and series resistance, *e.g.*, for a radius 10 μm we expect $f_{3\text{dB}} \sim 12$ GHz with the same device configuration.

CONCLUSIONS

We demonstrated a spectrally selective, free-space illuminated SLG/Si Schottky PDs at 1550 nm. The photodetection mechanism is based on internal photoemission at the SLG/Si interface. The photodetection is enhanced by integration in a F–P cavity and increasing the SLG absorption due to multiple reflections at the cavity resonance. As a result, we showed wavelength-dependent photoresponse with external (internal) responsivity ~ 20 mA/W (0.25A/W). The resonance wavelength may be further tuned by varying the Si cavity thickness, while the spectral selectivity can be increased by taking advantage of more complex high-finesse microcavities, which would provide both integrated spectral filtering and enhanced

SLG absorption. Our devices pave the way for developing high-responsivity graphene–Si free-space illuminated PDs for NIR.

METHODS

The devices are prepared as follows. A 100 nm thick SiO₂ layer is deposited on a 200 μm Si substrate by e-beam evaporation, Figure 3a, then patterned by optical lithography using a laser-writer (Microtech), followed by wet etching of SiO₂ in a buffer-oxide-etch (BOE) solution, Figure 3b. Next, Al ohmic contacts to the p-type Si are realized by an additional lithographic step, followed by lift-off and 30 min at 460 °C in a forming gas (5.7% H₂ in N₂), Figure 3c. To validate the Ohmic nature of the Al contact to Si after alloying we measure the I–V characteristics between Al/Si contacts from adjacent devices and confirm their linear behavior. To protect the Al pads from subsequent treatments involving HF, we cover Al with an Au layer using optical lithography, Cr/Au (3 nm/50 nm) evaporation and lift-off, Figure 3d. The ohmic contact imperfections (black spots) in Figure 1b arise from the Si/Al alloy process. This can be improved by increasing the thickness of the Al layer prior to alloying.

The CVD grown SLG is wet-transferred to the target chips, Figure 3e. The film is coated with 500 nm poly(methyl methacrylate) (PMMA), followed by Cu etching in ammonium persulfate (APS). The resulting SLG/PMMA film is rinsed in water to remove APS residuals. To obtain a SLG/Si Schottky interface without native oxide, we transfer SLG in diluted HF in deionized (DI) water (HF/DI water; 1:100).³⁶ After removing the APS residuals, the SLG/PMMA layer is placed in a plastic beaker containing 5 mL/500 mL HF and DI water. Next, the target substrate is first dipped in a buffered oxide etch (BOE) for 5s to etch the native Si oxide and then used to lift the floating SLG/PMMA layer. As a result, during drying, HF at the SLG/Si interface prevents Si oxidation.³⁶ After drying, the sample is placed in acetone to dissolve the PMMA, leaving the SLG covering the target substrate, Figure 3e.

After transfer, we use additional optical lithography steps to shape the SLG by oxygen plasma and then deposit Cr/Au (3 nm/50 nm) contacts by evaporation, followed by lift-off, Figure 2f. Before evaporation, a mild (0.5W, 20 s) Ar plasma (Moorfield NanoETCH) is applied on the exposed SLG areas to clean PMMA residuals, leading to a low (~100Ω) contact resistance at the metal–SLG interface, as estimated using a transfer length method. The bottom mirror consists of a 100 nm-thick-Au layer, thermally evaporated on the backside, Figure 3h.

Quality and uniformity of SLG is monitored by Raman spectroscopy using a Renishaw InVia equipped with a 100× objective at 514.5 nm and a laser power below 300 μW. Raman mapping is performed over a 100 μm × 140 μm area (pixel size 5 μm × 5 μm). At each position (pixel) we acquire Raman spectra from 1000 to 3000 cm⁻¹. A single Lorentzian fit is used to extract position and intensity of G and 2D peaks. Figure 5 plots the maps of Pos(G) and I(2D)/I(G) across the PD confirming that SLG is uniform in the photoactive SLG/Si Schottky junction (circular area, Figure 5).

For optoelectronic characterization we use light at telecom wavelengths from a tunable laser (ANDO AQ4321D). The optical signal is chopped and split between reference, used for continuous power monitoring, and device under test. The PD illumination is inspected by an IR camera. The photocurrent is amplified with a transimpedance amplifier (CVI Melles Griot 13AMP005) and fed to a lock-in amplifier (Signal Recovery 7280 SDP) for measuring the photoresponse. The incident optical power P_{inc} is measured separately with a InGaAs PD (Thorlabs DET410).

AUTHOR INFORMATION

Corresponding Author

*E-mail: acf26@eng.cam.ac.uk.

ORCID

Andrea C. Ferrari: 0000-0003-0907-9993

Notes

The authors declare no competing financial interest.

ACKNOWLEDGMENTS

We acknowledge funding from EU Graphene Flagship, ERC Grant Hetero2D, EPSRC Grants EP/K01711X/1, EP/K017144/1, EP/N010345/1, and EP/L016087/1.

REFERENCES

- (1) Agrawal, G. P. *Fiber-Optic Communication Systems*; John Wiley & Sons, 2012; Vol. 222.
- (2) Leitgeb, E.; Gebhart, M.; Birnbacher, U. Optical networks, last mile access and applications. In *Free-Space Laser Communications*; Springer: 2005; pp 273–302.
- (3) Kaushal, H.; Kaddoum, G. Optical communication in space: Challenges and mitigation techniques. *IEEE Commun. Surv. Tutorials* **2017**, *19* (1), 57–96.
- (4) Ijaz, M.; Ghassemlooy, Z.; Rajbhandari, S.; Le Minh, H.; Perez, J.; Gholami, A. Comparison of 830 and 1550 nm based free space optical communications link under controlled fog conditions, *8th International Symposium on Communication Systems, Networks & Digital Signal Processing (CSNDSP)*; IEEE, 2012; pp 1–5.
- (5) Flood, M. Laser altimetry: from science to commercial lidar mapping. *Photogramm. Eng. Remote Sens.* **2001**, *67* (11), 1209.
- (6) Parrish, C.; Osiri, R. In *Lidar Wavelength Considerations and Radiometric Performance Analysis for Coastal Applications*; AGU Fall, 2011.
- (7) Ishida, S.; Nishizawa, N. Quantitative comparison of contrast and imaging depth of ultrahigh-resolution optical coherence tomography images in 800–1700nm wavelength region. *Biomed. Opt. Express* **2012**, *3* (2), 282–294.
- (8) Sze, S. M.; Ng, K. K. *Physics of Semiconductor Devices*; John Wiley & Sons, 2006.
- (9) Eng, P. C.; Song, S.; Ping, B. State-of-the-art photodetectors for optoelectronic integration at telecommunication wavelength. *Nanophotonics* **2015**, *4* (3), 277–302.
- (10) Casalino, M.; Sirleto, L.; Moretti, L.; Della Corte, F.; Rendina, I. Design of a silicon resonant cavity enhanced photodetector based on the internal photoemission effect at 1.55 μm. *J. Opt. A: Pure Appl. Opt.* **2006**, *8* (10), 909.
- (11) Kang, Y.; Liu, H.-D.; Morse, M.; Paniccia, M. J.; Zadka, M.; Litski, S.; Sarid, G.; Pauchard, A.; Kuo, Y.-H.; Chen, H.-W. Monolithic germanium/silicon avalanche photodiodes with 340 GHz gain-bandwidth product. *Nat. Photonics* **2009**, *3* (1), 59–63.
- (12) Masini, G.; Cencelli, V.; Colace, L.; De Notaristefani, F.; Assanto, G. Monolithic integration of near-infrared Ge photodetectors with Si complementary metal-oxide-semiconductor readout electronics. *Appl. Phys. Lett.* **2002**, *80* (18), 3268–3270.
- (13) Koester, S. J.; Schaub, J. D.; Dehlinger, G.; Chu, J. O. Germanium-on-SOI infrared detectors for integrated photonic applications. *IEEE J. Sel. Top. Quantum Electron.* **2006**, *12* (6), 1489–1502.
- (14) Michel, J.; Liu, J.; Kimerling, L. C. High-performance Ge-on-Si photodetectors. *Nat. Photonics* **2010**, *4* (8), 527–534.
- (15) Assefa, S.; Xia, F.; Vlasov, Y. A. Reinventing germanium avalanche photodetector for nanophotonic on-chip optical interconnects. *Nature* **2010**, *464* (7285), 80–84.
- (16) Zhu, S.; Yu, M.; Lo, G.; Kwong, D. Near-infrared waveguide-based nickel silicide Schottky-barrier photodetector for optical communications. *Appl. Phys. Lett.* **2008**, *92* (8), 081103.
- (17) Goykhman, I.; Desiatov, B.; Khurgin, J.; Shappir, J.; Levy, U. Locally oxidized silicon surface-plasmon Schottky detector for telecom regime. *Nano Lett.* **2011**, *11* (6), 2219–2224.
- (18) Goykhman, I.; Desiatov, B.; Khurgin, J.; Shappir, J.; Levy, U. Waveguide based compact silicon Schottky photodetector with enhanced responsivity in the telecom spectral band. *Opt. Express* **2012**, *20* (27), 28594–28602.

- (19) Casalino, M.; Iodice, M.; Sirlito, L.; Rao, S.; Rendina, I.; Coppola, G. Low dark current silicon-on-insulator waveguide metal-semiconductor-metal-photodetector based on internal photoemissions at 1550 nm. *J. Appl. Phys.* **2013**, *114* (15), 153103.
- (20) Akbari, A.; Tait, R. N.; Berini, P. Surface plasmon waveguide Schottky detector. *Opt. Express* **2010**, *18* (8), 8505–8514.
- (21) Walden, R. H. A review of recent progress in InP-based optoelectronic integrated circuit receiver front-ends. *Int. J. High Speed Electron. Syst.* **1998**, *9* (02), 631–642.
- (22) Kang, Y.; Mages, P.; Clawson, A.; Yu, P.; Bitter, M.; Pan, Z.; Pauchard, A.; Hummel, S.; Lo, Y. Fused InGaAs-Si avalanche photodiodes with low-noise performances. *IEEE Photonics Technol. Lett.* **2002**, *14* (11), 1593–1595.
- (23) Sze, S. M. *VLSI Technology*, 2nd ed.; McGraw-Hill Education, 2003.
- (24) Lau, J. H. *Flip Chip Technologies*; McGraw-Hill: New York, 1995.
- (25) Harame, D.; Koester, S.; Freeman, G.; Cottrel, P.; Rim, K.; Dehlinger, G.; Ahlgren, D.; Dunn, J.; Greenberg, D.; Joseph, A. The revolution in SiGe: impact on device electronics. *Appl. Surf. Sci.* **2004**, *224* (1), 9–17.
- (26) Wang, J.; Lee, S. Ge-photodetectors for Si-based optoelectronic integration. *Sensors* **2011**, *11* (1), 696–718.
- (27) Peters, D. An infrared detector utilizing internal photoemission. *Proc. IEEE* **1967**, *55* (5), 704–705.
- (28) Brongersma, M. L.; Halas, N. J.; Nordlander, P. Plasmon-induced hot carrier science and technology. *Nat. Nanotechnol.* **2015**, *10* (1), 25–34.
- (29) Casalino, M. Internal photoemission theory: comments and theoretical limitations on the performance of near-infrared silicon schottky photodetectors. *IEEE J. Quantum Electron.* **2016**, *52* (4), 1–10.
- (30) Kimata, M.; Ueno, M.; Yagi, H.; Shiraishi, T.; Kawai, M.; Endo, K.; Kosabayama, Y.; Sone, T.; Ozeki, T.; Tsubouchi, N. PtSi Schottky-barrier infrared focal plane arrays. *Optoelectr. Rev.* **1998**, *1*–10.
- (31) Goykhman, I.; Desiatov, B.; Shappir, J.; Khurgin, J. B.; Levy, U. Model for quantum efficiency of guided mode plasmonic enhanced silicon Schottky detectors. arXiv preprint, arXiv:1401.2624, 2014.
- (32) Casalino, M.; Coppola, G.; De La Rue, R. M.; Logan, D. F. State-of-the-art all-silicon sub-bandgap photodetectors at telecom and datacom wavelengths. *Laser & Phot. Rev.* **2016**, *10* (6), 895–921.
- (33) Desiatov, B.; Goykhman, I.; Mazurski, N.; Shappir, J.; Khurgin, J. B.; Levy, U. Plasmonic enhanced silicon pyramids for internal photoemission Schottky detectors in the near-infrared regime. *Optica* **2015**, *2* (4), 335–338.
- (34) Amirmazlaghani, M.; Raissi, F.; Habibpour, O.; Vukusic, J.; Stake, J. Graphene-si schottky IR detector. *IEEE J. Quantum Electron.* **2013**, *49* (7), 589–594.
- (35) Wang, X.; Cheng, Z.; Xu, K.; Tsang, H. K.; Xu, J.-B. High-responsivity graphene/silicon-heterostructure waveguide photodetectors. *Nat. Photonics* **2013**, *7* (11), 888–891.
- (36) Goykhman, I.; Sassi, U.; Desiatov, B.; Mazurski, N.; Milana, S.; de Fazio, D.; Eiden, A.; Khurgin, J.; Shappir, J.; Levy, U. On-chip integrated, silicon-graphene plasmonic Schottky photodetector with high responsivity and avalanche photogain. *Nano Lett.* **2016**, *16* (5), 3005–3013.
- (37) An, X.; Liu, F.; Jung, Y. J.; Kar, S. Tunable graphene-silicon heterojunctions for ultrasensitive photodetection. *Nano Lett.* **2013**, *13* (3), 909–916.
- (38) Di Bartolomeo, A. Graphene Schottky diodes: An experimental review of the rectifying graphene/semiconductor heterojunction. *Phys. Rep.* **2016**, *606*, 1–58.
- (39) Chen, C.-C.; Aykol, M.; Chang, C.-C.; Levi, A.; Cronin, S. B. Graphene-silicon Schottky diodes. *Nano Lett.* **2011**, *11* (5), 1863–1867.
- (40) Ferrari, A. C.; Bonaccorso, F.; Fal'Ko, V.; Novoselov, K. S.; Roche, S.; BÅyggild, P.; Borini, S.; Koppens, F. H.; Palermo, V.; Pugno, N. Science and technology roadmap for graphene, related two-dimensional crystals, and hybrid systems. *Nanoscale* **2015**, *7* (11), 4598–4810.
- (41) Koppens, F.; Mueller, T.; Avouris, P.; Ferrari, A. C.; Vitiello, M.; Polini, M. Photodetectors based on graphene, other two-dimensional materials and hybrid systems. *Nat. Nanotechnol.* **2014**, *9* (10), 780–793.
- (42) Bonaccorso, F.; Sun, Z.; Hasan, T.; Ferrari, A. C. Graphene photonics and optoelectronics. *Nat. Photonics* **2010**, *4* (9), 611–622.
- (43) Sun, Z.; Hasan, T.; Torrisi, F.; Popa, D.; Privitera, G.; Wang, F.; Bonaccorso, F.; Basko, D. M.; Ferrari, A. C. Graphene mode-locked ultrafast laser. *ACS Nano* **2010**, *4* (2), 803–810.
- (44) Sorianello, V.; Midrio, M.; Contestabile, G.; Asselberg, I.; Van Campenhout, J.; Huyghebaerts, C.; Goykhman, I.; Ott, A.; Ferrari, A. C.; Romagnoli, M. Graphene Phase Modulator. arXiv preprint, arXiv:1704.01525, 2017.
- (45) Di Bartolomeo, A.; Luongo, G.; Giubileo, F.; Funicello, N.; Niu, G.; Schroeder, T.; Lisker, M.; Lupina, G. Hybrid graphene/silicon Schottky photodiode with intrinsic gating effect. *2D Mater.* **2017**, *4*, 025075.
- (46) Nair, R. R.; Blake, P.; Grigorenko, A. N.; Novoselov, K. S.; Booth, T. J.; Stauber, T.; Peres, N. M.; Geim, A. K. Fine structure constant defines visual transparency of graphene. *Science* **2008**, *320* (5881), 1308–1308.
- (47) Dawlaty, J. M.; Shivaraman, S.; Strait, J.; George, P.; Chandrashekar, M.; Rana, F.; Spencer, M. G.; Veksler, D.; Chen, Y. Measurement of the optical absorption spectra of epitaxial graphene from terahertz to visible. *Appl. Phys. Lett.* **2008**, *93* (13), 131905.
- (48) Muriel, M. A.; Carballar, A. Internal field distributions in fiber Bragg gratings. *IEEE Photonics Technol. Lett.* **1997**, *9* (7), 955–957.
- (49) Johnson, P. B.; Christy, R. W. Optical constants of the noble metals. *Phys. Rev. B* **1972**, *6* (12), 4370.
- (50) Falkovsky, L.; Pershoguba, S. Optical far-infrared properties of a graphene monolayer and multilayer. *Phys. Rev. B: Condens. Matter Mater. Phys.* **2007**, *76* (15), 153410.
- (51) Falkovsky, L.; Varlamov, A. Space-time dispersion of graphene conductivity. *Eur. Phys. J. B* **2007**, *56* (4), 281–284.
- (52) Saleh, B. E. A.; Teich, M. C. *Fundamentals of Photonics*; John Wiley & Sons, 1991.
- (53) Li, H. H. *J. Phys. Chem. Ref. Data* **1993**, *9*, 561.
- (54) Bae, S.; Kim, H.; Lee, Y.; Xu, X.; Park, J.-S.; Zheng, Y.; Balakrishnan, J.; Lei, T.; Kim, H. R.; Song, Y. I. Roll-to-roll production of 30-in. graphene films for transparent electrodes. *Nat. Nanotechnol.* **2010**, *5* (8), 574–578.
- (55) Lagatsky, A.; Sun, Z.; Kulmala, T.; Sundaram, R.; Milana, S.; Torrisi, F.; Antipov, O.; Lee, Y.; Ahn, J.; Brown, C. 2 μ m solid-state laser mode-locked by single-layer graphene. *Appl. Phys. Lett.* **2013**, *102* (1), 013113.
- (56) Ferrari, A. C.; Meyer, J.; Scardaci, V.; Casiraghi, C.; Lazzeri, M.; Mauri, F.; Piscanec, S.; Jiang, D.; Novoselov, K.; Roth, S. Raman spectrum of graphene and graphene layers. *Phys. Rev. Lett.* **2006**, *97* (18), 187401.
- (57) Temple, P. A.; Hathaway, C. Multiphonon Raman spectrum of silicon. *Phys. Rev. B* **1973**, *7* (8), 3685.
- (58) Ferrari, A. C.; Basko, D. M. Raman spectroscopy as a versatile tool for studying the properties of graphene. *Nat. Nanotechnol.* **2013**, *8* (4), 235–246.
- (59) Das, A.; Pisana, S.; Chakraborty, B.; Piscanec, S.; Saha, S.; Waghmare, U.; Novoselov, K.; Krishnamurthy, H.; Geim, A.; Ferrari, A. C. Monitoring dopants by Raman scattering in an electrochemically top-gated graphene transistor. *Nat. Nanotechnol.* **2008**, *3* (4), 210–215.
- (60) Basko, D.; Piscanec, S.; Ferrari, A. C. Electron-electron interactions and doping dependence of the two-phonon Raman intensity in graphene. *Phys. Rev. B: Condens. Matter Mater. Phys.* **2009**, *80* (16), 165413.
- (61) Bruna, M.; Ott, A. K.; Ijas, M.; Yoon, D.; Sassi, U.; Ferrari, A. C. Doping dependence of the Raman spectrum of defected graphene. *ACS Nano* **2014**, *8* (7), 7432–7441.

(62) Cancado, L. G.; Jorio, A.; Martins Ferreira, E.; Stavale, F.; Achete, C.; Capaz, R.; Moutinho, M.; Lombardo, A.; Kulmala, T.; Ferrari, A. C. Quantifying defects in graphene via Raman spectroscopy at different excitation energies. *Nano Lett.* **2011**, *11* (8), 3190–3196.

(63) Tongay, S.; Lemaitre, M.; Miao, X.; Gila, B.; Appleton, B.; Hebard, A. Rectification at graphene-semiconductor interfaces: zero-gap semiconductor-based diodes. *Phys. Rev. X* **2012**, *2* (1), 011002.

(64) Di Bartolomeo, A.; Giubileo, F.; Luongo, G.; Iemmo, L.; Martucciello, N.; Niu, G.; Frasccke, M.; Skibitzki, O.; Schroeder, T.; Lupina, G. Tunable Schottky barrier and high responsivity in graphene/Si-nanotip optoelectronic device. *2D Mater.* **2017**, *4*, 015024.

(65) Llopis, O.; Azaizia, S.; Saleh, K.; Ali Slimane, A.; Fernandez, A. Photodiode 1/f noise and other types of less known baseband noises in optical telecommunications devices. *IEEE Conf. Noise Fluct.* **2013**, *1*.

(66) Zhu, M.; Li, X.; Li, X.; Zang, X.; Zhen, Z.; Xie, D.; Fang, Y.; Zhu, H. Schottky diode characteristics and 1/f noise of high sensitivity reduced graphene oxide/Si heterojunction photodetector. *J. Appl. Phys.* **2016**, *119*, 124303.

(67) Selim Unlu, M.; Onat, B. M.; Leblebici, Y. Transient simulation of heterojunction photodiode-part II: Analysis of resonant cavity enhanced photodetectors. *J. Lightwave Technol.* **1995**, *13*, 406.